Circuit Modeling of a Wireless Power Transfer System Containing Ferrite Shields Using an Extended Impedance Expansion Method

Nozomi Haga, *Member, IEEE*, Jerdvisanop Chakarothai, *Senior Member, IEEE*, and Keisuke Konno, *Member, IEEE*

***Abstract*— The impedance expansion method (IEM) is a circuit modeling technique based on the method of moments (MoM). This study extended the conventional IEM to be applied to wireless power transfer (WPT) systems containing dielectric/magnetic (DM) bodies such as ferrites. The advantages of the extended IEM are that it can consider arbitrarily shaped DM bodies, self-resonant coils, and radiation loss, and that the equivalent electromagnetic currents on DM bodies are not treated as unknowns in the resulting circuit model. Numerical experiments revealed that the extended IEM is applicable up to the frequency at which the dimensions of the DM bodies are approximately 0.3 times the wavelength of electromagnetic waves inside the medium. An equivalent circuit model of a WPT system containing ferrite shields was obtained using the extended IEM and validated using the full-wave MoM and the finite-difference time-domain (FDTD) method.**

***Index Terms*— Dielectric materials, equivalent circuits, ferrites, magnetic materials, method of moments (MoM), wireless power transmission.**

I. Introduction

WIRELESS power transfer (WPT) technology has received significant attention because it can be used in various applications, including wireless charging of handheld devices and electric vehicles [1]. Generally, WPT systems consist of nonlinear electronic circuits (e.g., inverters and rectifiers) and wireless coupling elements (e.g., coils or electrodes). Therefore, an integrated design for an entire system using equivalent circuit models for coupling elements is effective for maximizing the power transfer efficiency of WPT systems [2]–[5].

Manuscript received August 1, 2021; revised October 29, 2021 and January 16, 2022; accepted January 30, 2022. Date of publication February 23, 2022; date of current version May 5, 2022. This work was supported by the Japan Society for the Promotion of Science Grants-in-Aid for Scientific Research (JSPS KAKENHI) under Grant 19K04321. *(Corresponding author: Nozomi Haga.)*

Nozomi Haga is with the Graduate School of Science and Technology, Gunma University, Kiryu 376-8515, Japan (e-mail: nozomi.haga@gunma-u.ac.jp).

Jerdvisanop Chakarothai is with the National Institute of Information and Communications Technology, Koganei 184-8795, Japan (e-mail: jerd@nict.go.jp).

Keisuke Konno is with the Department of Communications Engineering, Graduate School of Engineering, Tohoku University, Sendai 980-8579, Japan (e-mail: konno@ecei.tohoku.ac.jp).

Color versions of one or more figures in this article are available at https://doi.org/10.1109/TMTT.2022.3149830.

Digital Object Identifier 10.1109/TMTT.2022.3149830

To reduce electromagnetic interference in WPT systems, shields composed of magnetic bodies such as ferrites are often used [6]–[11]. For circuit modeling of such systems, the self- and mutual impedances between coils can be derived analytically by approximating the dimensions of the shields to infinity [7], [8]. However, this method cannot handle shields of finite dimensions and arbitrary shapes. Alternatively, the self- and mutual impedances between coils can be calculated numerically by finite-element eddy current analysis [9]–[11]. However, since this method is based on a low-frequency approximation, it cannot be applied to self-resonant coils [12] and cannot consider losses caused by electromagnetic radiation to infinite distance. Therefore, a new circuit modeling method that overcomes these problems is desired.

One candidate for such a requirement is the partial-element equivalent-circuit (PEEC) method [13], which is based on the mixed-potential integral equation and divides analysis objects into distributed capacitors and inductors. The PEEC method has been extended to consider dielectric/magnetic (DM) bodies, where volumetric polarization currents or surface equivalent electromagnetic currents on DM bodies are treated as unknowns in resulting circuit models [14], [15]. Therefore, the scale of the circuit models and the number of unknowns tend to be large, resulting in large memory consumption and limiting dimensions of analysis models.

Alternatively, the impedance expansion method (IEM) [16], [17], which is a circuit modeling method based on the method of moments (MoM) [18], [19], is a candidate for the same purpose. The advantages of the IEM are that it can model self-resonant coils and radiation losses [20], and that the derived distributed-element models can be reduced to lumped-element models in combination with eigenmode analysis, which also reduces the number of unknowns when performing wideband frequency response analysis [21].

The IEM was first applied to WPT systems in free space and then extended to consider scattering by perfect conductors [22]. This study further extends the IEM to consider scattering by lossless DM bodies, such as ferrite shields for WPT systems used in megahertz regions. Whereas the conventional IEMs including [22] are based only on the electric field integral equation, the IEM extended in this study adopts the Poggio–Miller–Chang–Harrington–Wu–Tsai (PMCHWT) integral equations [23], which has the advantage of being

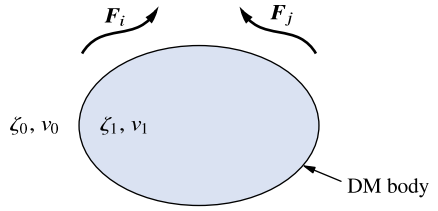

Fig. 1. Basis functions $\boldsymbol{F}_i$ and $\boldsymbol{F}_j$ in the vicinity of a DM body.

applicable not only to WPT systems including ferrite shields but also to various systems such as capacitive coupling WPT systems mounted on dielectric substrates.

Unlike the PEEC method, the extended IEM includes contribution from scattering by DM bodies in the self- and mutual impedances between basis functions on coupling elements. Therefore, the equivalent electromagnetic currents on DM bodies are not treated as unknowns in the resulting circuit model, which reduces the total number of unknowns in circuit equations. This is an advantage of the extended IEM compared with the PEEC method.

The remainder of this article is organized as follows. Section II describes the theory of the extended IEM. Section III evaluates the applicable frequency of the extended IEM. Section IV demonstrates the circuit modeling of a WPT system containing ferrite shields. Section V summarizes our conclusion.

In this article, the vector functions are denoted by bold italic type (e.g., $\boldsymbol{F}$), the algebraic vectors are denoted by bold roman type (e.g., $\mathbf{I}$), and the algebraic matrices are denoted by bold roman type with an overbar (e.g., $\bar{\mathbf{Z}}$).

II. Theory

As mentioned in Section I, the theory proposed in this article is an extension of that proposed in [22], so there are many similarities between their derivation processes. However, for convenience, this section prioritizes completeness of description.

A. Basic Concept

As shown in Fig. 1, two basis functions $\boldsymbol{F}_i$ and $\boldsymbol{F}_j$, which represent electric currents on conductors placed in the vicinity of a single DM body, such as ferrites, are considered. The generalization to the case of multiple DM bodies is straightforward, so only the derivation for the case with a single DM body will be described. The wave impedance and speed of light outside the DM body are ζ_0 and v_0, respectively, and those inside the DM body are ζ_1 and v_1, respectively. The self-/mutual impedance between $\boldsymbol{F}_i$ and $\boldsymbol{F}_j$ is denoted as Z_{ij} and can be separated as follows:

$$Z_{ij} = Z_{ij}^{\mathrm{fs}} + Z_{ij}^{\mathrm{sc}}. \tag{1}$$

The free-space component Z_{ij}^{fs} is the self-/mutual impedance in the absence of the DM body, and the scattering component Z_{ij}^{sc} is the component induced by scattering by the DM body.

B. Free-Space Components

The free-space component Z_{ij}^{fs} can be expanded into the Laurent series with respect to the complex angular frequency s as follows:

$$Z_{ij}^{\mathrm{fs}} = \sum_{k=-1}^{\infty} s^k Z_{ij}^{\mathrm{fs}(k)}. \tag{2}$$

The coefficient $Z_{ij}^{\mathrm{fs}(k)}$ is expressed as follows [16]:

$$Z_{ij}^{\mathrm{fs}(k)} = \frac{\zeta_0}{v_0^k} X\left(\boldsymbol{F}_i, \boldsymbol{F}_j, k\right) \tag{3}$$

$$X(\boldsymbol{F}_i, \boldsymbol{F}_j, -1) = \int_S \int_S \frac{(\nabla \cdot \boldsymbol{F}_i)\left(\nabla' \cdot \boldsymbol{F}_j'\right)}{4\pi R} dS' dS \tag{4}$$

$$X(\boldsymbol{F}_i, \boldsymbol{F}_j, 0) = 0 \tag{5}$$

$$X(\boldsymbol{F}_i, \boldsymbol{F}_j, k) = (-1)^{k+1} \int_S \int_S \left[\frac{\boldsymbol{F}_i \cdot \boldsymbol{F}_j' R^{k-2}}{(k-1)!4\pi} + \frac{(\nabla \cdot \boldsymbol{F}_i)\left(\nabla' \cdot \boldsymbol{F}_j'\right) R^k}{(k+1)!4\pi} \right] \times dS' dS, \quad k \geq 1 \tag{6}$$

where S is the surface region of the conducting and DM bodies, and R is the distance between the source coordinate $\boldsymbol{r}'$ and observation coordinate $\boldsymbol{r}$, meaning $R = |\boldsymbol{r} - \boldsymbol{r}'|$. The functions, operators, and surface elements with respect to $\boldsymbol{r}'$ are denoted by primes. Additionally, if $\nabla \cdot \boldsymbol{F}_i = 0 \vee \nabla \cdot \boldsymbol{F}_j = 0$, then

$$X\left(\boldsymbol{F}_i, \boldsymbol{F}_j, -1\right) = 0 \tag{7}$$

$$X\left(\boldsymbol{F}_i, \boldsymbol{F}_j, 2\right) = 0. \tag{8}$$

Therefore, $Z_{ij}^{\mathrm{fs}(-1)} = Z_{ij}^{\mathrm{fs}(2)} = 0$. The result in (7) is obvious according to (4) and (8) was proven in [16] and [22].

C. Matrix Equations for Equivalent Currents

In the remainder of this section, the method for obtaining the scattering component Z_{ij}^{sc} in the expanded form is described. As will be discussed in Section II-E, the extended IEM also requires solving linear equations with coefficient matrices for static fields. These matrices are rank-deficient (ill-conditioned) if the well-known rooftop [24] or Rao–Wilton–Glisson [25] basis functions are used. To avoid the low-frequency breakdown problem, the surface equivalent electric and magnetic current densities $\boldsymbol{J}_d$ and $\boldsymbol{M}_d$ on the DM body are expanded into the loop-star basis functions [26], [27] as follows:

$$\boldsymbol{J}_d = \sum_{j=1}^{N_\star} I_j^\star \boldsymbol{F}_j^\star + \sum_{j=1}^{N_\circ} I_j^\circ \boldsymbol{F}_j^\circ \tag{9}$$

$$\boldsymbol{M}_d = \sum_{j=1}^{N_\star} V_j^\star \boldsymbol{F}_j^\star + \sum_{j=1}^{N_\circ} V_j^\circ \boldsymbol{F}_j^\circ \tag{10}$$

where $\boldsymbol{F}_j^\star$ and $\boldsymbol{F}_j^\circ$ are the ith star and loop basis functions, respectively (the latter of which satisfies $\nabla \cdot \boldsymbol{F}_j^\circ = 0$), $N_\star$ and $N_\circ$ are the number of star and loop basis functions, respectively, and I_j^υ and V_j^υ are the electric and magnetic current coefficients for $\boldsymbol{F}_j^\upsilon$, respectively ($\upsilon = \star, \circ$).

Here, we assume that a source electric current $I_j \boldsymbol{F}_j$ induces an electromagnetic field around the DM body, where I_j is the electric current coefficient for $\boldsymbol{F}_j$. By substituting (9) and (10) into the PMCHWT electric and magnetic integral equations

and applying the Galerkin testing procedure with the star and loop basis functions, the following matrix equations can be obtained:

$$\begin{bmatrix} \bar{\mathbf{Z}}_{\star\star} & \bar{\mathbf{U}}_{\star\circ} \\ \bar{\mathbf{U}}_{\circ\star} & -\bar{\mathbf{Y}}_{\circ\circ} \end{bmatrix} \begin{bmatrix} \mathbf{I}_\star \\ \mathbf{V}_\circ \end{bmatrix} + \begin{bmatrix} \bar{\mathbf{Z}}_{\star\circ} & \bar{\mathbf{U}}_{\star\star} \\ \bar{\mathbf{U}}_{\circ\circ} & -\bar{\mathbf{Y}}_{\circ\star} \end{bmatrix} \begin{bmatrix} \mathbf{I}_\circ \\ \mathbf{V}_\star \end{bmatrix} = -\begin{bmatrix} \mathbf{Z}_{\star j} \\ \mathbf{U}_{\circ j} \end{bmatrix} I_j \tag{11}$$

$$\begin{bmatrix} \bar{\mathbf{Z}}_{\circ\star} & \bar{\mathbf{U}}_{\circ\circ} \\ \bar{\mathbf{U}}_{\star\star} & -\bar{\mathbf{Y}}_{\star\circ} \end{bmatrix} \begin{bmatrix} \mathbf{I}_\star \\ \mathbf{V}_\circ \end{bmatrix} + \begin{bmatrix} \bar{\mathbf{Z}}_{\circ\circ} & \bar{\mathbf{U}}_{\circ\star} \\ \bar{\mathbf{U}}_{\star\circ} & -\bar{\mathbf{Y}}_{\star\star} \end{bmatrix} \begin{bmatrix} \mathbf{I}_\circ \\ \mathbf{V}_\star \end{bmatrix} = -\begin{bmatrix} \mathbf{Z}_{\circ j} \\ \mathbf{U}_{\star j} \end{bmatrix} I_j. \tag{12}$$

The matrices and vectors in (11) and (12) are defined below ($\tau, \upsilon = \star, \circ$).

- $\bar{\mathbf{Z}}_{\tau\upsilon}$ $N_\tau \times N_\upsilon$ impedance matrix, whose (i, j)th element is the self-/mutual impedance between $\boldsymbol{F}_i^\tau$ and $\boldsymbol{F}_j^\upsilon$.
- $\bar{\mathbf{Y}}_{\tau\upsilon}$ $N_\tau \times N_\upsilon$ admittance matrix, whose (i, j)th element is the self-/mutual admittance between $\boldsymbol{F}_i^\tau$ and $\boldsymbol{F}_j^\upsilon$.
- $\bar{\mathbf{U}}_{\tau\upsilon}$ $N_\tau \times N_\upsilon$ transfer matrix, whose (i, j)th element is the transfer coefficient between $\boldsymbol{F}_i^\tau$ and $\boldsymbol{F}_j^\upsilon$.
- $\mathbf{Z}_{\tau j}$ $N_\tau \times 1$ impedance vector, whose ith element is the mutual impedance between $\boldsymbol{F}_i^\tau$ and $\boldsymbol{F}_j$.
- $\mathbf{U}_{\tau j}$ $N_\tau \times 1$ transfer vector, whose ith element is the transfer coefficient between $\boldsymbol{F}_i^\tau$ and $\boldsymbol{F}_j$.
- $\mathbf{I}_\tau$ $N_\tau \times 1$ electric current vector, whose ith element is the electric current coefficient I_i^τ for $\boldsymbol{F}_i^\tau$.
- $\mathbf{V}_\tau$ $N_\tau \times 1$ magnetic current vector, whose ith element is the magnetic current coefficient V_i^τ for $\boldsymbol{F}_i^\tau$.

D. Laurent Series Expansion of Matrices and Vectors

Similar to Z_{ij}^{fs}, the matrices and vectors in (11) and (12) can be expanded as follows ($\tau, \upsilon = \star, \circ$):

$$\left.\begin{aligned} \bar{\mathbf{Z}}_{\tau\upsilon} &= \sum_{k=-1}^{\infty} s^k \bar{\mathbf{Z}}_{\tau\upsilon}^{(k)}, \quad \bar{\mathbf{Y}}_{\tau\upsilon} = \sum_{k=-1}^{\infty} s^k \bar{\mathbf{Y}}_{\tau\upsilon}^{(k)} \\ \bar{\mathbf{U}}_{\tau\upsilon} &= \sum_{k=0}^{\infty} s^k \bar{\mathbf{U}}_{\tau\upsilon}^{(k)} \\ \mathbf{Z}_{\tau j} &= \sum_{k=-1}^{\infty} s^k \mathbf{Z}_{\tau j}^{(k)}, \quad \mathbf{U}_{\tau j} = \sum_{k=0}^{\infty} s^k \mathbf{U}_{\tau j}^{(k)} \end{aligned}\right\}. \tag{13}$$

The (i, j)th elements of $\bar{\mathbf{Z}}_{\tau\upsilon}^{(k)}, \bar{\mathbf{Y}}_{\tau\upsilon}^{(k)}$, and $\bar{\mathbf{U}}_{\tau\upsilon}^{(k)}$ and the ith elements of $\mathbf{Z}_{\tau j}^{(k)}$ and $\mathbf{U}_{\tau j}^{(k)}$ are expressed as follows ($\tau, \upsilon = \star, \circ$):

$$\left[\bar{\mathbf{Z}}_{\tau\upsilon}^{(k)}\right]_{ij} = \left(\frac{\zeta_0}{\upsilon_0^k} + \frac{\zeta_1}{\upsilon_1^k}\right) X\left(\boldsymbol{F}_i^\tau, \boldsymbol{F}_j^\upsilon, k\right) \tag{14}$$

$$\left[\bar{\mathbf{Y}}_{\tau\upsilon}^{(k)}\right]_{ij} = \left(\frac{1}{\zeta_0 \upsilon_0^k} + \frac{1}{\zeta_1 \upsilon_1^k}\right) X\left(\boldsymbol{F}_i^\tau, \boldsymbol{F}_j^\upsilon, k\right) \tag{15}$$

$$\left[\bar{\mathbf{U}}_{\tau\upsilon}^{(k)}\right]_{ij} = \left(\frac{1}{\upsilon_0^k} + \frac{1}{\upsilon_1^k}\right) W\left(\boldsymbol{F}_i^\tau, \boldsymbol{F}_j^\upsilon, k\right) \tag{16}$$

$$\left[\mathbf{Z}_{\tau j}^{(k)}\right]_i = \frac{\zeta_0}{\upsilon_0^k} X\left(\boldsymbol{F}_i^\tau, \boldsymbol{F}_j, k\right) \tag{17}$$

$$\left[\mathbf{U}_{\tau j}^{(k)}\right]_i = \frac{1}{\upsilon_0^k} W\left(\boldsymbol{F}_i^\tau, \boldsymbol{F}_j, k\right) \tag{18}$$

$$W(\boldsymbol{F}_i, \boldsymbol{F}_j, k) = (1-k)(-1)^k \times \int_S \int_S \frac{(\boldsymbol{F}_i \times \boldsymbol{F}_j') \cdot (\boldsymbol{r} - \boldsymbol{r}') R^{k-3}}{k! 4\pi} dS' dS. \tag{19}$$

According to (19), it is clear that

$$W(\boldsymbol{F}_i, \boldsymbol{F}_j, 1) = 0. \tag{20}$$

Additionally, if $\nabla \cdot \boldsymbol{F}_i = \nabla \cdot \boldsymbol{F}_j = 0$, then

$$W(\boldsymbol{F}_i, \boldsymbol{F}_j, 0) = 0 \tag{21}$$

$$W(\boldsymbol{F}_i, \boldsymbol{F}_j, 3) = 0 \tag{22}$$

where (21) holds because the magnetic fields yielded by solenoidal (divergence-free) electric currents are irrotational [26] and (22) is proven in the Appendix.

Note that the following relationships hold because of (5), (7), (8), and (20)–(46) ($\tau, \upsilon = \star, \circ$):

$$\bar{\mathbf{Z}}_{\tau\upsilon}^{(0)} = \bar{\mathbf{Y}}_{\tau\upsilon}^{(0)} = \bar{\mathbf{U}}_{\tau\upsilon}^{(1)} = \bar{\mathbf{0}}, \tag{23}$$

$$\mathbf{Z}_{\tau j}^{(0)} = \mathbf{U}_{\tau j}^{(1)} = \mathbf{Z}_{\circ j}^{(-1)} = \mathbf{Z}_{\circ j}^{(2)} = \mathbf{0}. \tag{24}$$

Additionally, if $\tau = \circ \vee \upsilon = \circ$, then

$$\bar{\mathbf{Z}}_{\tau\upsilon}^{(-1)} = \bar{\mathbf{Z}}_{\tau\upsilon}^{(2)} = \bar{\mathbf{Y}}_{\tau\upsilon}^{(-1)} = \bar{\mathbf{Y}}_{\tau\upsilon}^{(2)} = \bar{\mathbf{0}}. \tag{25}$$

Furthermore, if $\nabla \cdot \boldsymbol{F}_j = 0$, then

$$\mathbf{Z}_{\star j}^{(-1)} = \mathbf{Z}_{\star j}^{(2)} = \mathbf{U}_{\circ j}^{(0)} = \mathbf{U}_{\circ j}^{(3)} = \mathbf{0}. \tag{26}$$

The electric and magnetic current vectors in (11) and (12) are expanded as follows ($\upsilon = \star, \circ$):

$$\mathbf{I}_\upsilon = \sum_{k=0}^{\infty} s^k \mathbf{I}_\upsilon^{(k)}, \quad \mathbf{V}_\upsilon = \sum_{k=-1}^{\infty} s^k \mathbf{V}_\upsilon^{(k)} \tag{27}$$

where it is assumed that $\mathbf{V}_\star^{(-1)} = \mathbf{V}_\star^{(0)} = \mathbf{0}$.

E. Matrix Equations for Expanded Equivalent Currents

By substituting (13) and (27) into (11) and (12), and extracting the terms with the same power of s, the following matrix equations can be obtained ($k = 0, 1, \ldots$):

$$\begin{aligned} &\begin{bmatrix} \bar{\mathbf{Z}}_{\star\star}^{(-1)} & \bar{\mathbf{U}}_{\star\circ}^{(0)} \\ \bar{\mathbf{U}}_{\circ\star}^{(0)} & -\bar{\mathbf{Y}}_{\circ\circ}^{(1)} \end{bmatrix} \begin{bmatrix} \mathbf{I}_\star^{(k)} \\ \mathbf{V}_\circ^{(k-1)} \end{bmatrix} \\ &\quad = -\begin{bmatrix} \mathbf{Z}_{\star j}^{(k-1)} \\ \mathbf{U}_{\circ j}^{(k)} \end{bmatrix} I_j - \sum_{l=2}^{k} \begin{bmatrix} \bar{\mathbf{Z}}_{\star\star}^{(l-1)} & \bar{\mathbf{U}}_{\star\circ}^{(l)} \\ \bar{\mathbf{U}}_{\circ\star}^{(l)} & -\bar{\mathbf{Y}}_{\circ\circ}^{(l+1)} \end{bmatrix} \begin{bmatrix} \mathbf{I}_\star^{(k-l)} \\ \mathbf{V}_\circ^{(k-l-1)} \end{bmatrix} \\ &\qquad - \sum_{l=2}^{k} \begin{bmatrix} \bar{\mathbf{Z}}_{\star\circ}^{(l-1)} & \bar{\mathbf{U}}_{\star\star}^{(l-2)} \\ \bar{\mathbf{U}}_{\circ\circ}^{(l)} & -\bar{\mathbf{Y}}_{\circ\star}^{(l-1)} \end{bmatrix} \begin{bmatrix} \mathbf{I}_\circ^{(k-l)} \\ \mathbf{V}_\star^{(k-l+1)} \end{bmatrix} \end{aligned} \tag{28}$$

$$\begin{aligned} &\begin{bmatrix} \bar{\mathbf{Z}}_{\circ\circ}^{(1)} & \bar{\mathbf{U}}_{\circ\star}^{(0)} \\ \bar{\mathbf{U}}_{\star\circ}^{(0)} & -\bar{\mathbf{Y}}_{\star\star}^{(-1)} \end{bmatrix} \begin{bmatrix} \mathbf{I}_\circ^{(k)} \\ \mathbf{V}_\star^{(k+1)} \end{bmatrix} \\ &\quad = -\begin{bmatrix} \mathbf{Z}_{\circ j}^{(k+1)} \\ \mathbf{U}_{\star j}^{(k)} \end{bmatrix} I_j - \sum_{l=0}^{k} \begin{bmatrix} \bar{\mathbf{Z}}_{\circ\star}^{(l+1)} & \bar{\mathbf{U}}_{\circ\circ}^{(l+2)} \\ \bar{\mathbf{U}}_{\star\star}^{(l)} & -\bar{\mathbf{Y}}_{\star\circ}^{(l+1)} \end{bmatrix} \begin{bmatrix} \mathbf{I}_\star^{(k-l)} \\ \mathbf{V}_\circ^{(k-l-1)} \end{bmatrix} \\ &\qquad - \sum_{l=2}^{k} \begin{bmatrix} \bar{\mathbf{Z}}_{\circ\circ}^{(l+1)} & \bar{\mathbf{U}}_{\circ\star}^{(l)} \\ \bar{\mathbf{U}}_{\star\circ}^{(l)} & -\bar{\mathbf{Y}}_{\star\star}^{(l-1)} \end{bmatrix} \begin{bmatrix} \mathbf{I}_\circ^{(k-l)} \\ \mathbf{V}_\star^{(k-l+1)} \end{bmatrix}. \end{aligned} \tag{29}$$

As mentioned in Section II-C, the matrices on the left-hand sides of (28) and (29) are for static fields, regardless of k. If $\mathbf{I}_\star^{(0)}, \ldots, \mathbf{I}_\star^{(k-2)}$, $\mathbf{I}_\circ^{(0)}, \ldots, \mathbf{I}_\circ^{(k-2)}$, $\mathbf{V}_\star^{(1)}, \ldots, \mathbf{V}_\star^{(k-1)}$, and $\mathbf{V}_\circ^{(-1)}, \ldots, \mathbf{V}_\circ^{(k-3)}$ are known, (28) can be solved for $\mathbf{I}_\star^{(k)}$ and $\mathbf{V}_\circ^{(k-1)}$. Using $\mathbf{I}_\star^{(k)}$ and $\mathbf{V}_\circ^{(k-1)}$, (29) can then be solved for

$\mathbf{I}_{\circ}^{(k)}$ and $\mathbf{V}_{\star}^{(k+1)}$. This process is performed sequentially for $k = 0, 1, \ldots$ According to (23)–(25), (28), and (29), the following components in (27) are zero as follows:

$$\mathbf{I}_{\star}^{(1)} = \mathbf{I}_{\circ}^{(1)} = \mathbf{V}_{\star}^{(2)} = \mathbf{V}_{\circ}^{(0)} = \mathbf{0}. \tag{30}$$

Additionally, according to (26), if $\nabla \cdot \boldsymbol{F}_j = 0$, then

$$\mathbf{I}_{\star}^{(0)} = \mathbf{I}_{\star}^{(3)} = \mathbf{V}_{\circ}^{(-1)} = \mathbf{V}_{\circ}^{(2)} = \mathbf{0}. \tag{31}$$

F. Testing Scattered Electric Fields

The equivalent electric and magnetic currents $\boldsymbol{J}_d$ and $\boldsymbol{M}_d$ yield a scattered electric field $\boldsymbol{E}^{\mathrm{sc}}$. By testing $\boldsymbol{E}^{\mathrm{sc}}$ by $\boldsymbol{F}_i$, the scattering impedance component Z_{ij}^{sc} can be obtained as follows:

$$\begin{aligned} Z_{ij}^{\mathrm{sc}} &= -\frac{1}{I_j}\int_S \boldsymbol{F}_i \cdot \boldsymbol{E}^{\mathrm{sc}} dS \\ &= \frac{1}{I_j}\left\{ \begin{bmatrix} \mathbf{Z}_{i\star} & \mathbf{U}_{i\circ} \end{bmatrix} \begin{bmatrix} \mathbf{I}_{\star} \\ \mathbf{V}_{\circ} \end{bmatrix} + \begin{bmatrix} \mathbf{Z}_{i\circ} & \mathbf{U}_{i\star} \end{bmatrix} \begin{bmatrix} \mathbf{I}_{\circ} \\ \mathbf{V}_{\star} \end{bmatrix} \right\}. \end{aligned} \tag{32}$$

The parameters in (32) are defined below ($\upsilon = \star, \circ$).

- $\mathbf{Z}_{i\upsilon}$ $1 \times N_\upsilon$ impedance vector, whose jth element is the mutual impedance between $\boldsymbol{F}_i$ and $\boldsymbol{F}_j^{\upsilon}$.
- $\mathbf{U}_{i\upsilon}$ $1 \times N_\upsilon$ transfer vector, whose jth element is the transfer coefficient between $\boldsymbol{F}_i$ and $\boldsymbol{F}_j^{\upsilon}$.

The vectors in (32) can be expanded as follows ($\upsilon = \star, \circ$):

$$\mathbf{Z}_{i\upsilon} = \sum_{k=-1}^{\infty} s^k \mathbf{Z}_{i\upsilon}^{(k)}, \quad \mathbf{U}_{i\upsilon} = \sum_{k=0}^{\infty} s^k \mathbf{U}_{i\upsilon}^{(k)} \tag{33}$$

where the following components are zero:

$$\mathbf{Z}_{i\upsilon}^{(0)} = \mathbf{U}_{i\upsilon}^{(1)} = \mathbf{Z}_{i\circ}^{(-1)} = \mathbf{Z}_{i\circ}^{(2)} = \mathbf{0}. \tag{34}$$

Additionally, if $\nabla \cdot \boldsymbol{F}_i = 0$, then

$$\mathbf{Z}_{i\star}^{(-1)} = \mathbf{Z}_{i\star}^{(2)} = \mathbf{U}_{i\circ}^{(0)} = \mathbf{U}_{i\circ}^{(3)} = \mathbf{0}. \tag{35}$$

By substituting (27) and (33) into (32), the expanded form of Z_{ij}^{sc} can be obtained as follows:

$$Z_{ij}^{\mathrm{sc}} = \sum_{k=-1}^{\infty} s^k Z_{ij}^{\mathrm{sc}(k)} \tag{36}$$

where

$$\begin{aligned} Z_{ij}^{\mathrm{sc}(k)} = \frac{1}{I_j}\Bigg\{ &\sum_{l=-1}^{k} \begin{bmatrix} \mathbf{Z}_{i\star}^{(l)} & \mathbf{U}_{i\circ}^{(l+1)} \end{bmatrix} \begin{bmatrix} \mathbf{I}_{\star}^{(k-l)} \\ \mathbf{V}_{\circ}^{(k-l-1)} \end{bmatrix} \\ &+ \sum_{l=1}^{k} \begin{bmatrix} \mathbf{Z}_{i\circ}^{(l)} & \mathbf{U}_{i\star}^{(l-1)} \end{bmatrix} \begin{bmatrix} \mathbf{I}_{\circ}^{(k-l)} \\ \mathbf{V}_{\star}^{(k-l+1)} \end{bmatrix} \Bigg\}. \end{aligned} \tag{37}$$

According to (30) and (34), the equality of $Z_{ij}^{\mathrm{sc}(0)} = 0$ holds in general. Additionally, based on (31) and (35), one can prove that $Z_{ij}^{\mathrm{sc}(-1)} = Z_{ij}^{\mathrm{sc}(2)} = 0$ if $\nabla \cdot \boldsymbol{F}_i = 0 \vee \nabla \cdot \boldsymbol{F}_j = 0$.

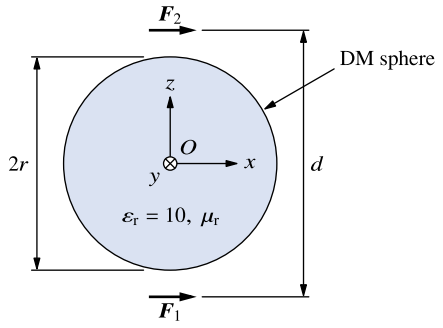

Fig. 2. Basis functions $\boldsymbol{F}_1$ and $\boldsymbol{F}_2$ in the vicinity of a DM sphere.

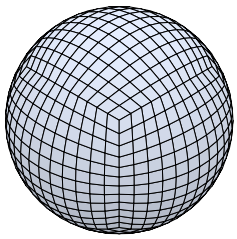

Fig. 3. DM sphere divided into quadrangular faces.

III. Applicable Frequency of the Extended IEM

To evaluate the applicable frequency of the extended IEM, the scattering component of the mutual impedance between two basis functions in the vicinity of a DM sphere was evaluated. As shown in Fig. 2, the sphere has a radius r, relative permittivity $\varepsilon_r = 10$, and relative permeability μ_r. As shown in Fig. 3, the sphere is divided into 864 quadrangular faces. Each of the equivalent electric and magnetic currents $\boldsymbol{J}_d$ and $\boldsymbol{M}_d$ on the sphere is expanded into $N_\star = 863$ star basis functions and $N_\circ = 865$ loop basis functions, each of which is a linear combination of modified rooftop basis functions [20]. Two filamentary piecewise linear basis functions $\boldsymbol{F}_1$ and $\boldsymbol{F}_2$ with a length of 10 mm are defined at $z = \mp d/2$ on the z-axis and parallel to the x-axis.

The expanded form of the scattering component Z_{21}^{sc} was compared with the full-waveform, which can be obtained by solving (11) and (12) for $\mathbf{I}_\star, \mathbf{I}_\circ, \mathbf{V}_\star$, and $\mathbf{V}_\circ$, and substituting the results into (32). The error in Z_{21}^{sc} is defined as follows:

$$\mathrm{Error} = \left| \tilde{Z}_{21}^{\mathrm{sc}} / Z_{21}^{\mathrm{sc}} - 1 \right| \tag{38}$$

where Z_{21}^{sc} is the scattering component derived by the full-wave MoM and $\tilde{Z}_{21}^{\mathrm{sc}}$ is derived from the extended IEM in the Laurent series of finite degree L, meaning

$$\tilde{Z}_{21}^{\mathrm{sc}} = \sum_{k=-1}^{L} s^k Z_{21}^{\mathrm{sc}(k)}. \tag{39}$$

Fig. 4 shows the frequency dependence of the error in Z_{21}^{sc} at various values of L, where $r = 80$ mm, $\mu_r = 40$, and $d = 200$ mm. It can be seen that the error increases with frequency, and the increase after a certain frequency is rapid. This frequency is higher for a greater degree L of the Laurent series. As a result, the error exceeds 10^{-4} at approximately

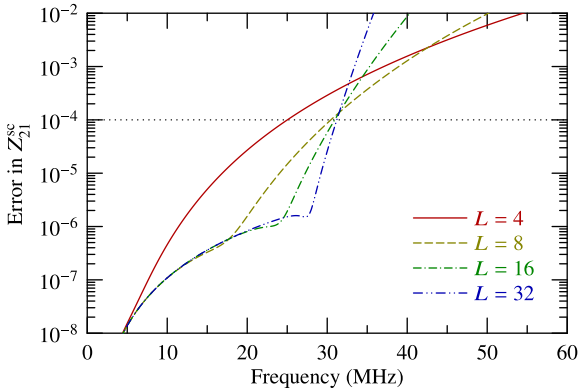

Fig. 4. Frequency dependence of the error in Z_{21}^{sc} at various values of L, where $r = 80$ mm, $\mu_r = 40$, and $d = 200$ mm.

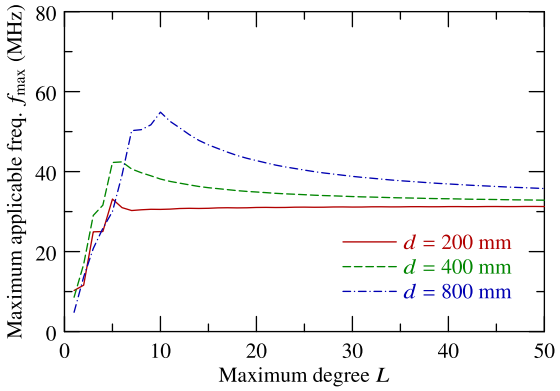

Fig. 5. f_{max} as a function of L at various d, where $r = 80$ mm and $\mu_r = 40$.

31 MHz, regardless of L. In this case, it can be concluded that the extended IEM is applicable up to approximately 31 MHz.

Based on the results described above, the maximum applicable frequency f_{max} is defined as the frequency at which the error in Z_{21}^{sc} exceeds the tolerance of 10^{-4}. Fig. 5 shows f_{max} as a function of L at various d, where $r = 80$ mm and $\mu_r = 40$. In the range of $L \leq 5$, f_{max} increases as L increases, and then converges to approximately 31–36 MHz. Because the rate of change of the convergence frequency is small compared with that of d, the convergence frequency is expected to depend mainly on factors other than the positions of basis functions.

To clarify how the convergence frequency is determined, Fig. 6 shows f_{max} as a function of μ_r (10–100) at $L = 50$, where $r = 80$ mm and $d = 200$ mm. The values approximately follow the solid curve, which represents the frequency at which $r = 0.167\lambda_1$, where λ_1 is the wavelength of electromagnetic waves inside the sphere. Fig. 7 shows f_{max} as a function of r (40–80 mm) at $L = 50$, where $\mu_r = 40$ and $d = 200$ mm. Similar to the previous case, f_{max} approximately follows the frequency at which $r = 0.167\lambda_1$.

Additionally, it has been confirmed that f_{max} for arbitrarily shaped DM bodies that fit on a sphere of radius r is greater than that for a DM sphere of radius r with the same permittivity and permeability. Therefore, the extended IEM is considered to be applicable up to the frequency at which the

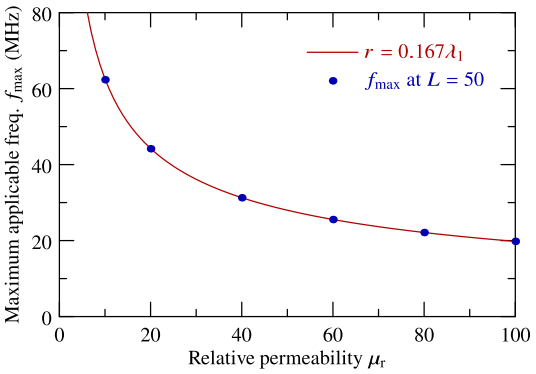

Fig. 6. f_{max} as a function of μ_r at $L = 50$, where $r = 80$ mm and $d = 200$ mm.

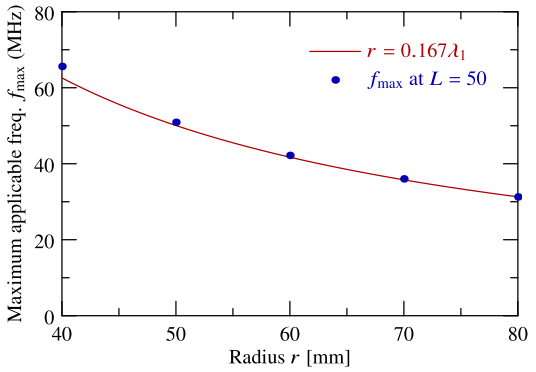

Fig. 7. f_{max} as a function of r at $L = 50$, where $\mu_r = 40$ and $d = 200$ mm.

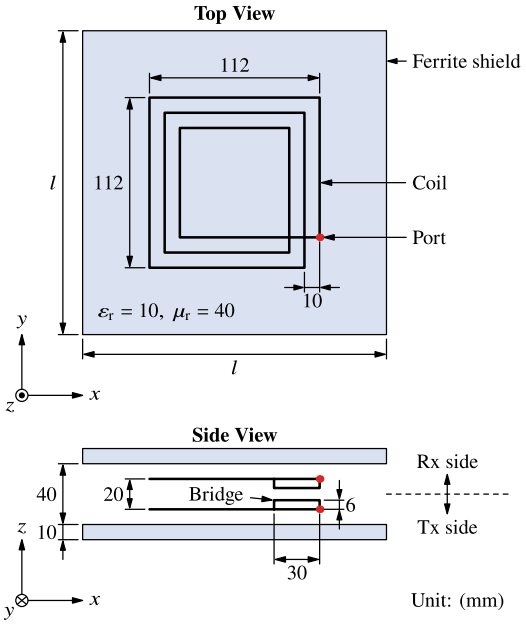

Fig. 8. WPT system containing ferrite shields.

dimensions of DM bodies are approximately 0.3 times the wavelength inside the medium.

IV. Circuit Modeling of WPT System Containing Ferrite Shields

A. Analysis Model

Fig. 8 shows the WPT system analyzed in this study. The transmitting (Tx) and receiving (Rx) coils have a square shape

and three windings. The bridges connecting the outermost and innermost windings are 6 mm in height, and Tx and Rx ports are provided between the bridge and outermost winding. The port impedance consists of a pure resistance R_0 in series with a matching capacitor C_0. The available power at the Tx port is 1 W. The wires forming the coils have a radius $r = 0.4$ mm and conductivity $\sigma = 58$ MS/m. The internal impedance per unit length of the wires, which is denoted as ζ_c, can be expressed as follows [28]:

$$\zeta_c = \frac{k_c}{2\pi\sigma r}\frac{J_0(k_c r)}{J_1(k_c r)} \tag{40}$$

where $k_c = (-s\mu_0\sigma)^{1/2}$ is the wavenumber, and J_0 and J_1 are the Bessel functions of the first kind with orders of zero and one, respectively. The coils are sandwiched between two square ferrite shields with a side length l, thickness 10 mm, relative permittivity $\varepsilon_r = 10$, and relative permeability $\mu_r = 40$. The Tx and Rx sides are symmetric about the xy-plane. In the case of $l = 200$ mm, which is the largest size considered in this study, the ferrite shields fit on a sphere with a radius of approximately 145 mm. Therefore, the extended IEM can be applied up to at least approximately 17.3 MHz. The ferrite shields are assumed to be lossless based on the limitations of the extended IEM. If a magnetic loss tangent of 0.01 is considered, which is a realistic value for modern ferrites for megahertz band, the full-wave MoM confirmed that there is little effect on the S-parameters and conduction loss, although there is an error of approximately 10 dB in the radiation loss. The precise consideration of material loss in the IEM is a future issue to be explored.

The currents of the Tx and Rx coils are approximated to be infinitely thin and uniform along the wire axes, meaning they are solenoidal. The surface of each ferrite shield is divided into rectangular faces. In the case of $l = 200$ mm, $N_\star = 2015$ star basis functions and $N_\circ = 2017$ loop basis functions are assigned to the faces and nodes, respectively. It has been confirmed that even if the number of unknowns varies between -50% and $+40\%$, the difference in the resulting circuit parameters is less than 6%. By applying the extended IEM, the self- and mutual impedances between the Tx and Rx coils can be obtained in the following form:

$$Z_{ij} = \sum_{k=1}^{4} s^k Z_{ij}^{(k)}, \quad i, j = 1, 2 \tag{41}$$

where Z_{11} and Z_{22} are the self-impedances of the Tx and Rx coils, respectively, and $Z_{21} = Z_{12}$ is the mutual impedance between the coils. Here, $Z_{ij}^{(-1)} = Z_{ij}^{(2)} = 0$ because the currents are assumed to be solenoidal.

B. Derived Circuit Model

Fig. 9 shows the derived circuit model of the WPT system. V_0 is the electromotive force of the Tx port. I_1 and I_2 are the currents on the Tx and Rx coils, respectively. The inductances represent the impedance components proportional to s as

$$L_{ij} = Z_{ij}^{(1)}, \quad i, j = 1, 2. \tag{42}$$

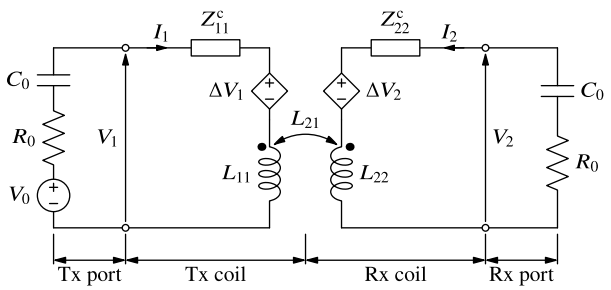

Fig. 9. Circuit model of the WPT system.

TABLE I
CIRCUIT PARAMETERS WITH AND WITHOUT FERRITE SHIELDS ($l = 200$ mm)

	w/o shields	w/ shields
$L_{11} = L_{22}$ [H]	1.608×10^{-6}	2.335×10^{-6}
L_{21} [H]	5.704×10^{-7}	1.193×10^{-6}
$Z_{11}^{(3)} = Z_{22}^{(3)}$ [$\Omega\cdot$s^3]	-1.117×10^{-26}	-4.973×10^{-26}
$Z_{21}^{(3)}$ [$\Omega\cdot$s^3]	-1.045×10^{-26}	-4.742×10^{-26}
$Z_{11}^{(4)} = Z_{22}^{(4)}$ [$\Omega\cdot$s^4]	1.659×10^{-36}	1.911×10^{-36}
$Z_{21}^{(4)}$ [$\Omega\cdot$s^4]	1.659×10^{-36}	1.890×10^{-36}
$Z_{11}^c = Z_{22}^c$ [Ω]	$0.3114 + j0.3014$	

The dependent voltage sources ΔV_1 and ΔV_2 represent the voltage drops caused by higher degree impedance components and are expressed as follows:

$$\Delta V_i = \sum_{j=1}^{2}\sum_{k=3}^{4} s^k Z_{ij}^{(k)} I_j, \quad i = 1, 2. \tag{43}$$

The radiation loss P_r can be obtained as follows:

$$P_r = \sum_{i=1}^{2}\sum_{j=1}^{2}\sum_{k=1}^{2} s^{2k} Z_{ij}^{(2k)} I_i^* I_j. \tag{44}$$

The impedances Z_{11}^c and Z_{22}^c in Fig. 9 are the internal impedances of the Tx and Rx coils, respectively, and they can be obtained by multiplying ζ_c by the total length of the wire. The conduction loss P_c can be obtained as follows:

$$P_c = \sum_{i=1}^{2} \mathrm{Re}\left(Z_{ii}^c\right)|I_i|^2. \tag{45}$$

Table I summarizes the numerical parameters of the circuit model with and without ferrite shields with $l = 200$ mm. The value of $Z_{11}^c = Z_{22}^c$ in Table I is for 6.78 MHz, and it differs for other frequencies. The presence of ferrite shields increases the self- and mutual inductances by 45% and 109%, respectively. This means that the coupling coefficient L_{21}/L_{11} increases by 44%. The impedance components proportional to s^3 increases by 350% based on the presence of ferrite shields. However, assuming a frequency of 6.78 MHz, we have $sL_{11} = j99.47\ \Omega$ and $s^3 Z_{11}^{(3)} = j3.845\ \mathrm{m}\Omega$, indicating that the contributions of the impedance components proportional to s^3 are negligible. The impedance components proportional to s^4 correspond to the radiation resistances of infinitesimal

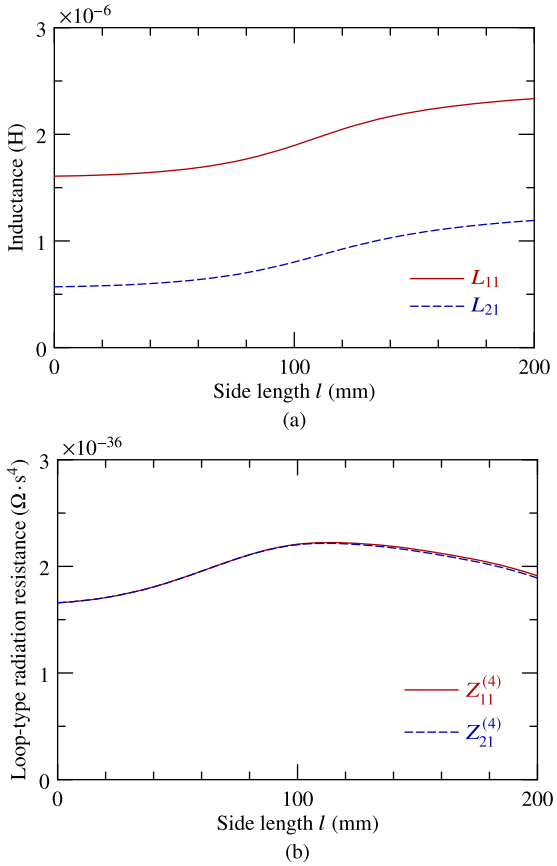

Fig. 10. Dependencies of (a) inductances and (b) loop-type radiation resistances on the side length l.

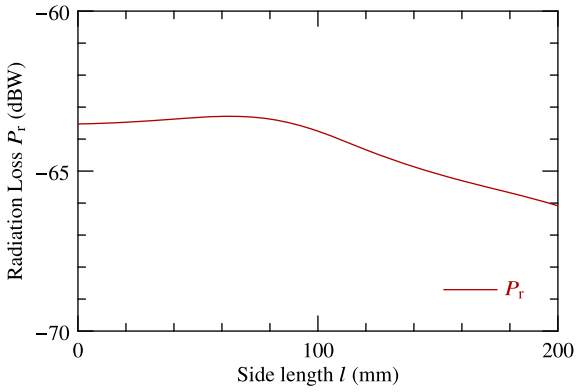

Fig. 11. Dependence of the radiation loss P_r on the side length l, where R_0 and C_0 are matched to the conjugate image impedance of the coils at 6.78 MHz.

loop currents [20] and are referred to as "loop-type radiation resistances" in this article. They increase by approximately 15% based on the presence of ferrite shields. Regardless, their increase is relatively small compared with those of the self- and mutual inductances (45% and 109%, respectively). Therefore, it is suggested that radiation loss can be suppressed by ferrite shields for a given Tx power.

To investigate the effects of ferrite shields on the circuit parameters and radiation loss further, Fig. 10 shows the dependencies of the inductances and loop-type radiation resistances on the side length l. Additionally, Fig. 11 shows the dependence of radiation loss P_r on the side length l, where R_0 and C_0 are matched to the conjugate image impedance [29] of the coils at 6.78 MHz. The self- and mutual inductances increase monotonically as l increases from 0 to 200 mm. On the other hand, the loop-type radiation resistances take the maximum values when the side length l is comparable to the dimensions of the coils. Consequently, the radiation loss P_r in Fig. 11 is approximately constant in the range of $l < 80$ mm and decreases with an increasing l in the range of $l > 80$ mm.

C. Validity of the Circuit Model

To validate the derived circuit model, the S-parameters and radiation and conduction losses calculated by the circuit model were compared with those calculated by the full-wave MoM and finite-difference time-domain (FDTD) method [30].

In the full-wave MoM, each coil is divided into 125 linear segments, and the current of each coil is expanded into a single uniform loop current and 124 piecewise linear basis functions. The ferrite shields are discretized in the same manner as in the IEM.

In the FDTD method, the minimum and maximum cell sizes are 2 and 5 mm, respectively, and the time step is 3.84 ps. The spaces around the wires and inside the ferrite shields are discretized into cubic cells with dimensions of 2 mm × 2 mm × 2 mm. The wires are composed of distributed resistors whose resistance per unit length is equal to the real part of ζ_c at 6.78 MHz. The dimensions of the computational domain are 400 mm × 400 mm × 400 mm, and the domain is surrounded by a 32-layer perfectly matched layer (PML). The domain including the PML was divided into 7 640 480 voxels. The Tx coil was excited by a Gaussian derivative pulse with a frequency spectrum of −60 dB at 40 MHz. The number of calculation iterations was set to 1 000 000 so that the currents of the coils were attenuated to −140 dB relative to the peak values. The radiation loss cannot be calculated accurately by the FDTD method based on the limited performance of PML at low frequencies. Therefore, it was calculated using only the derived circuit model and full-wave MoM.

Fig. 12 shows the frequency dependencies of the reflection coefficient $|S_{11}|$, transmission coefficient $|S_{21}|$, radiation loss P_r, and conduction loss P_c with ferrite shields, where $l = 200$ mm, $R_0 = 50\ \Omega$, and $C_0 = 274.6$ pF. The slight difference between $|S_{11}|$ calculated by the circuit model and full-wave MoM can be attributed to the fact that the current of each loop is approximated to be uniform in the circuit model. P_c calculated by the FDTD method is only consistent with those calculated by the other methods at approximately 6.78 MHz. This is because the internal impedance of the wires is approximated by pure resistances that are independent of the frequency in the FDTD method. Regardless, the results calculated by each method are generally in good agreement. Therefore, the circuit model derived by the extended IEM can be considered to be valid.

D. Computational Cost

Finally, the memory usage and computational times required for the FDTD method, full-wave MoM, and extended IEM were compared. To measure computational time, a workstation

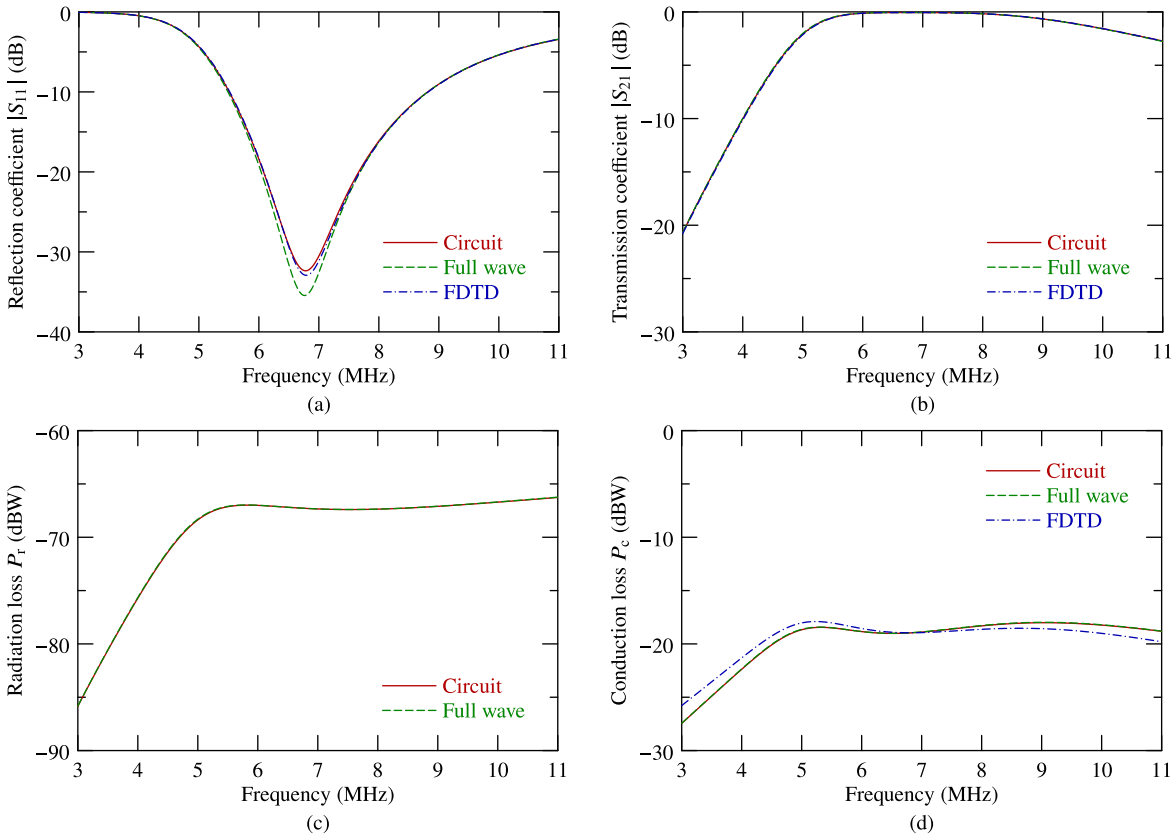

Fig. 12. Frequency dependencies of (a) reflection coefficient $|S_{11}|$, (b) transmission coefficient $|S_{21}|$, (c) radiation loss P_r, and (d) conduction loss P_c with ferrite shields, where $l = 200$ mm, $R_0 = 50\ \Omega$, and $C_0 = 274.6$ pF.

with a 4 GHz quad-core CPU and 32 GB 2666 MHz RAM was considered. Whereas the memory required for the FDTD method is approximately 0.49 GB (assuming single-precision data), the minimum memory required to store the coefficient matrices is approximately 4 GB for the full-wave MoM and approximately 10 GB for the extended IEM (assuming double-precision data). The high memory usage in the extended IEM is a natural consequence of the expansion of the coefficient matrices. However, the extended IEM is far superior to the other methods in terms of computational time, as described below. In the FDTD method, the computational time required for 1 000 000 iterations was approximately 90 195 s. For the full-wave MoM, the computational time per frequency was approximately 639 s (606 s for matrix filling and 33 s for LU decomposition). In contrast, the extended IEM only required approximately 459 s to obtain the circuit parameters [454 s for filling the matrices in (13) and (33) and 5 s for (28), (29), and (37)]. The subsequent frequency sweep required approximately 52 μs per frequency. Therefore, almost no additional time is required for multiple frequency points, demonstrating the high computational efficiency of the extended IEM for the analysis of WPT system with ferrite shields when compared with the FDTD method and full-wave MoM.

The above trend in computational cost also holds for other analysis objects. In the extended IEM, the memory usage and computational time required for filling matrices in (13) and (33) are proportional to L (the degree of the Laurent series), and the computational time required for (28), (29), and (37) is proportional to L^2. If the number of unknowns is the same and the direct method is used to solve (28) and (29), the computational time does not depend on the shape of the analysis object. For example, in the case of the problem addressed in Section III, the computational time per frequency for the full-wave MoM is approximately 72.38 s, whereas the computational time required to obtain the scattering components in the extended IEM is approximately 54.63 s for $L = 4$ and approximately 67.14 s for $L = 8$. Furthermore, the computational time required for the frequency sweep in the extended IEM is approximately 22 μs for $L = 4$ and approximately 40 μs for $L = 8$ (per frequency), which is negligible compared with that in the full-wave MoM. This result further supports the advantage of the extended IEM.

V. Conclusion

In this study, the IEM was extended to consider scattering by lossless DM bodies. Numerical experiments demonstrated that the extended IEM is applicable up to the frequency at which the dimensions of DM bodies are approximately 0.3 times the wavelength inside the medium. A circuit model of a WPT system containing ferrite shields was derived using the extended IEM. The effects of ferrite shields on the increase in the coupling coefficient and reduction in the radiation loss were confirmed. Additionally, the results calculated by the circuit model were consistent with those obtained by the

full-wave MoM and FDTD method, which supports the validity of the derived circuit model. Furthermore, the extended IEM was demonstrated to be far superior to the FDTD method and full-wave MoM in terms of computational time. To further validate the applicability of the extended IEM to actual WPT systems, actual measurements will be conducted in future studies.

Appendix
Proof Regarding Expanded Transfer Coefficient

The coefficient $W(\boldsymbol{F}_i, \boldsymbol{F}_j, 3)$ can be rewritten as follows:

$$\begin{aligned} W(\boldsymbol{F}_i, \boldsymbol{F}_j, 3) &= \int_S \int_S \frac{(\boldsymbol{F}_i \times \boldsymbol{F}'_j) \cdot (\boldsymbol{r} - \boldsymbol{r}')}{12\pi} dS' dS \\ &= \frac{1}{12\pi} \left[\left(\int_S \boldsymbol{r} \times \boldsymbol{F}_i dS \right) \cdot \left(\int_S \boldsymbol{F}'_j dS' \right) \right. \\ &\quad \left. + \left(\int_S \boldsymbol{F}_i dS \right) \cdot \left(\int_S \boldsymbol{r}' \times \boldsymbol{F}'_j dS' \right) \right]. \end{aligned} \tag{46}$$

If $\nabla \cdot \boldsymbol{F}_i = \nabla \cdot \boldsymbol{F}_j = 0$, then the following relationship holds:

$$\int_S \boldsymbol{F}_i dS = \int_S \boldsymbol{F}'_j dS' = \boldsymbol{0}. \tag{47}$$

By substituting (47) into (46), the equality of $W(\boldsymbol{F}_i, \boldsymbol{F}_j, 3) = 0$ can be proven.

Acknowledgment

This work was performed in the Cooperative Research Project of the Research Institute of Electrical Communication, Tohoku University.

References

[1] N. Shinohara, *Wireless Power Transfer: Theory, Technology, and Applications*. Stevenage, U.K.: IET, 2018.

[2] T. Nagashima, X. Wei, E. Bou, E. Alarcón, M. K. Kazimierczuk, and H. Sekiya, "Analysis and design of loosely inductive coupled wireless power transfer system based on class-E^2 DC-DC converter for efficiency enhancement," *IEEE Trans. Circuits Syst. I, Reg. Paper*, vol. 62, no. 11, pp. 2781–2791, Nov. 2015, doi: 10.1109/TCSI.2015.2482338.

[3] T. Imura and Y. Hori, "Maximizing air gap and efficiency of magnetic resonant coupling for wireless power transfer using equivalent circuit and Neumann formula," *IEEE Trans. Ind. Electron.*, vol. 58, no. 10, pp. 4746–4752, Oct. 2011, doi: 10.1109/TIE.2011.2112317.

[4] N. Inagaki, "Theory of image impedance matching for inductively coupled power transfer systems," *IEEE Trans. Microw. Theory Techn.*, vol. 62, no. 4, pp. 901–908, Apr. 2014, doi: 10.1109/TMTT.2014.2300033.

[5] N. Ha-Van and C. Seo, "Analytical and experimental investigations of omnidirectional wireless power transfer using a cubic transmitter," *IEEE Trans. Ind. Electron.*, vol. 65, no. 2, pp. 1358–1366, Feb. 2018, doi: 10.1109/TIE.2017.2733470.

[6] S. Kong *et al.*, "An investigation of electromagnetic radiated emission and interference from multi-coil wireless power transfer systems using resonant magnetic field coupling," *IEEE Trans. Microw. Theory Techn.*, vol. 63, no. 3, pp. 833–846, Mar. 2015, doi: 10.1109/TMTT.2015.2392096.

[7] W. G. Hurley and M. C. Duffy, "Calculation of self- and mutual impedances in planar sandwich inductors," *IEEE Trans. Magn.*, vol. 33, no. 3, pp. 2282–2290, May 1997, doi: 10.1109/20.573844.

[8] S. Jeong, "Smartwatch strap wireless power transfer system with flexible PCB coil and shielding material," *IEEE Trans. Ind. Electron.*, vol. 66, no. 5, pp. 4054–4064, May 2019, doi: 10.1109/TIE.2018.2860534.

[9] Z. Li, C. Zhu, J. Jiang, K. Song, and G. Wei, "A 3-kW wireless power transfer system for sightseeing car supercapacitor charge," *IEEE Trans. Power Electron.*, vol. 32, no. 5, pp. 3301–3316, May 2017, doi: 10.1109/TPEL.2016.2584701.

[10] M. Mohammad, E. T. Wodajo, S. Choi, and M. E. Elbuluk, "Modeling and design of passive shield to limit EMF emission and to minimize shield loss in unipolar wireless charging system for EV," *IEEE Trans. Power Electron.*, vol. 34, no. 12, pp. 12235–12245, Dec. 2019, doi: 10.1109/TPEL.2019.2903788.

[11] M. E. Bima, I. Bhattacharya, and C. W. V. Neste, "Experimental evaluation of layered DD coil structure in a wireless power transfer system," *IEEE Trans. Electromagn. Compat.*, vol. 62, no. 4, pp. 1477–1484, Aug. 2020, doi: 10.1109/TEMC.2020.3002694.

[12] A. Karalis, J. D. Joannopoulos, and M. Soljačić, "Efficient wireless non-radiative mid-range energy transfer," *Ann. Phys.*, vol. 323, no. 1, pp. 34–48, 2008, doi: 10.1016/j.aop.2007.04.017.

[13] A. E. Ruehli, G. Antonini, and L. Jiang, *Circuit Oriented Electromagnetic Modeling Using the PEEC Techniques*. New York, NY, USA: Wiley, 2017.

[14] A. E. Ruehli and H. Heeb, "Circuit models for three-dimensional geometries including dielectrics," *IEEE Trans. Microw. Theory Techn.*, vol. 40, no. 7, pp. 1507–1516, Jul. 1992, doi: 10.1109/22.146332.

[15] D. Gope, A. E. Ruehli, C. Yang, and V. Jandhyala, "(S)PEEC: Time- and frequency-domain surface formulation for modeling conductors and dielectrics in combined circuit electromagnetic simulations," *IEEE Trans. Microw. Theory Techn.*, vol. 54, no. 6, pp. 2453–2464, Jun. 2006, doi: 10.1109/TMTT.2006.875796.

[16] N. Haga and M. Takahashi, "Circuit modeling technique for electrically-very-small devices based on Laurent series expansion of self-/mutual impedances," *IEICE Trans. Commun.*, vol. E101.B, no. 2, pp. 555–563, Feb. 2018, doi: 10.1587/transcom.2017EBP3196.

[17] N. Haga and M. Takahashi, "Passive element approximation of equivalent circuits by the impedance expansion method," *IEICE Trans. Commun.*, vol. E101-B, no. 4, pp. 1069–1075, Apr. 2018, doi: 10.1587/transcom.2017EBP3246.

[18] R. F. Harrington, *Field Computation by Moment Methods*. New York, NY, USA: Macmillan, 1965.

[19] W. C. Gibson, *The Method of Moments in Electromagnetics*, 2nd ed. Boca Raton, FL, USA: CRC Press, 2014.

[20] N. Haga and M. Takahashi, "Analysis of a wireless power transfer system by the impedance expansion method using Fourier basis functions," *IEICE Trans. Commun.*, vol. E101.B, no. 7, pp. 1708–1715, Jul. 2018, doi: 10.1587/transcom.2017EBP3316.

[21] N. Haga and M. Takahashi, "Circuit modeling of a wireless power transfer system by eigenmode analysis based on the impedance expansion method," *IEEE Trans. Antennas Propag.*, vol. 67, no. 2, pp. 1233–1245, Feb. 2019, doi: 10.1109/TAP.2018.2883632.

[22] N. Haga, J. Chakarothai, and K. Konno, "Circuit modeling of wireless power transfer system in the vicinity of perfectly conducting scatterer," *IEICE Trans. Commun.*, vol. E103.B, no. 12, pp. 1411–1420, Dec. 2020, doi: 10.1587/transcom.2019EBP3211.

[23] K. Umashankar, A. Taflove, and S. M. Rao, "Electromagnetic scattering by arbitrary shaped three-dimensional homogeneous lossy dielectric objects," *IEEE Trans. Antennas Propag.*, vol. AP-34, no. 6, pp. 758–766, Jun. 1986, doi: 10.1109/TAP.1986.1143894.

[24] A. W. Glisson and D. Wilton, "Simple and efficient numerical methods for problems of electromagnetic radiation and scattering from surfaces," *IEEE Trans. Antennas Propag.*, vol. AP-28, no. 5, pp. 593–603, Sep. 1980, doi: 10.1109/TAP.1980.1142390.

[25] S. M. Rao, D. R. Wilton, and A. W. Glisson, "Electromagnetic scattering by surfaces of arbitrary shape," *IEEE Trans. Antennas Propag.*, vol. AP-30, no. 3, pp. 409–418, May 1982, doi: 10.1109/TAP.1982.1142818.

[26] S. Y. Chen, W. C. Chew, J. M. Song, and J.-S. Zhao, "Analysis of low frequency scattering from penetrable scatterers," *IEEE Trans. Geosci. Remote Sens.*, vol. 39, no. 4, pp. 726–735, Apr. 2001, doi: 10.1109/36.917883.

[27] S. Chen, J.-S. Zhao, and W. C. Chew, "Analyzing low-frequency electromagnetic scattering from a composite object," *IEEE Trans. Geosci. Remote Sens.*, vol. 40, no. 2, pp. 426–433, Feb. 2002, doi: 10.1109/36.992806.

[28] W. L. Weeks, *Transmission and Distribution of Electrical Energy*. New YorkA, NY, USA: Harper & Row, 1981.

[29] S. Roberts, "Conjugate-image impedances," *Proc. IRE*, vol. 34, no. 4, pp. 198–204, Apr. 1946, doi: 10.1109/JRPROC.1946.234242.

[30] A. Taflove and S. C. Hagness, *Computational Electrodynamics: The Finite-Difference Time-Domain Method*, 3rd ed. Norwood, MA, USA: Artech House, 2005.

Nozomi Haga (Member, IEEE) was born in Yamagata, Japan, in January 1985. He received the B.E., M.E., and D.E. degrees from Chiba University, Chiba, Japan, in 2007, 2009, and 2012, respectively.

He is currently an Assistant Professor at Gunma University, Gunma, Japan. His main interests have been electrically small antennas, body-centric wireless communication channels, and wireless power transfer systems.

Dr. Haga received the Institute of Electronics, Information and Communication Engineers (IEICE) Technical Committee on Antennas and Propagation: Young Researcher Award in 2012, the IEICE Technical Committee on Wireless Power Transfer: Young Researcher Award in 2018, and the IEEE Antennas and Propagation Society Japan Young Engineer Award in 2018.

Jerdvisanop Chakarothai (Senior Member, IEEE) received the B.E. degree in electrical and electronic engineering from Akita University, Akita, Japan, in 2003, and the M.E. and D.E. degrees in electrical and communications engineering from Tohoku University, Sendai, Japan, in 2005 and 2010, respectively.

He has been a Research Associate at Tohoku University since 2010, prior to joining the Nagoya Institute of Technology, Nagoya, Japan, and Tokyo Metropolitan University, Tokyo, Japan, in 2011 and 2013, respectively. He is currently with the National Institute of Information and Communications Technology, Tokyo. His research interests include computational electromagnetics (CEM) for biomedical communications and electromagnetic compatibility, and measurement and calibration methods for electromagnetic interference.

Dr. Chakarothai is a member of the Institute of Electronics, Information and Communication Engineers (IEICE) and the Institute of Electrical Engineers (IEE), Japan. He is also a member of the Bioelectromagnetic Society and the Applied Computational Electromagnetic Society. He received the Young Scientist Award from the International Scientific Radio Union in 2014 and the Ulrich L. Rohde Innovative Conference Paper Award on Antenna Measurements and Applications in 2018.

Keisuke Konno (Member, IEEE) received the B.E., M.E., and D.E. degrees from Tohoku University, Sendai, Japan, in 2007, 2009, and 2012, respectively.

Since 2012, he has been with the Department of Communications Engineering, Graduate School of Engineering, Tohoku University, where he is an Associate Professor. He received a Japan Society for the Promotion of Science (JSPS) Post-Doctoral Fellowship for Research Abroad and he was staying with the ElectroScience Laboratory, The Ohio State University, Columbus, OH, USA, as a Visiting Scholar, from 2015 to 2017. His research interests include computational electromagnetics, array antennas, reflectarrays, and source reconstruction.

Dr. Konno is a member of the Institute of Electronics, Information and Communication Engineers (IEICE). He received the Encouragement Award for Young Researcher and Most Frequent Presentations Award in 2010 from the Technical Committee on Antennas and Propagation of Japan, the Young Researchers Award in 2011 from the IEICE of Japan, the IEEE Electromagnetic Compatibility (EMC) Society Sendai Chapter Student Brush-Up Session and EMC Sendai Seminar Student Best Presentation Award in 2011, the JSPS Washington Director Award in 2016, the MHz Rectenna Award in 2017, the Young Researchers Award for Group of Electrical Engineering, Communication Engineering, Electronic Engineering, and Information Engineering (ECEI) of Tohoku University in 2018, the Minoru Ishida Award in 2018, the IEEE Antennas and Propagation Society (AP-S) Japan Young Engineer Award in 2018, and TOKIN Foundation Research Encouragement Award in 2019.